Article

Robust MPPT Control of Stand-Alone Photovoltaic Systems via Adaptive Self-Adjusting Fractional Order PID Controller

Omer Saleem [1], Shehryaar Ali [2] and Jamshed Iqbal [3,*]

1   Department of Electrical Engineering, National University of Computer and Emerging Sciences, Lahore 54770, Pakistan
2   Department of Electrical Engineering, School of Electrical Engineering and Computer Science, National University of Science and Technology, Islamabad 44000, Pakistan
3   School of Computer Science, Faculty of Science and Engineering, University of Hull, Hull HU6 7RX, UK
*   Correspondence: j.iqbal@hull.ac.uk

Abstract: The Photovoltaic (PV) system is an eco-friendly renewable energy system that is integrated with a DC-DC buck-boost converter to generate electrical energy as per the variations in solar irradiance and outdoor temperature. This article proposes a novel Adaptive Fractional Order PID (A-FOPID) compensator with self-adjusting fractional orders to extract maximum power from a stand-alone PV system as ambient conditions change. The reference voltage is generated using a feed-forward neural network. The conventional FOPID compensator, which operates on the output voltage error of the interleaved buck-boost converter, is employed as the baseline maximum-power-point-tracking (MPPT) controller. The baseline controller is retrofitted with an online state-error-driven adaptation law that dynamically modifies the fractional orders of the controller's integral and differential operators. The adaptation law is formulated as a nonlinear hyperbolic scaling function of the system's state error and error-derivative variables. This augmentation supplements the controller's adaptability, enabling it to manipulate flexibly the tightness of the applied control effort as the operating conditions change. The efficacy of the proposed control law is analyzed by carrying out customized simulations in the MATLAB Simulink environment. The simulation results show that the proposed MPPT control scheme yields a mean improvement of 25.4% in tracking accuracy and 11.3% in transient response speed under varying environmental conditions.

Keywords: photovoltaic system; buck-boost converter; maximum power extraction; fractional order PID control; self-adjusting orders; online adaptation law

1. Introduction

With the rapid advancement in science and technology, the global demand for electrical energy is continuously increasing [1]. Presently, the majority of electrical energy demand is fulfilled by the consumption of fossil fuels [2]. However, the fossil fuel reserves are limited and will eventually run out. Apart from their exhaustive nature, the utilization of fossil fuels adversely affects the environment by increasing pollution and causing greenhouse effects, which lead to global warming. The aforementioned limitations associated with fossil fuels necessitate the utilization of renewable energy resources as a safe and clean alternative to contribute to global energy production and eventually replace non-renewable sources [3]. Solar Photovoltaic (PV) energy systems are widely preferred over other renewable energy systems owing to their environment-friendly nature, reasonable conversion efficiency, ease of commissioning, minimal maintenance expenses, zero fuel consumption, and silent operation [4]. PV systems are generally used in either standalone or grid-connected configurations. Standalone PV systems supply electricity to customers who are either far from the power grid or have low energy requirements [5]. Grid-connected systems generate energy to fulfill their local requirements and feed the excess to the main electrical grid [6].

The output of PV systems depends on the prevailing atmospheric conditions, such as ambient temperature and solar irradiance [7,8]. The changes in these parameters due to the climatic conditions as well as the sun's movement throughout the day greatly affect the output energy of PV systems. Extracting the maximum amount of available energy from the installed PV system is indeed a challenging problem for scientists and researchers [9]. A well-postulated maximum power point tracking (MPPT) control system enhances the conversion efficiency of the PV system by as much as 98% [10]. Extensive work has been conducted to devise reliable MPPT control schemes.

1.1. Literature Review

Extensive work has been conducted and correspondingly, several reliable MPPT controller variants have been proposed in the open scientific literature [11,12]. Conventionally, the perturb-and-observe technique and the incremental conductance technique have been used to generate reference trajectories in MPPT applications owing to their computational simplicity [13,14]. However, these techniques lack the ability to effectively compensate for the abrupt variations in solar irradiance and steady-state oscillations. Hence, the Feedforward Neural Network (FNN) and other similar soft computing techniques have gained a lot of popularity recently owing to their design flexibility [9]. The Proportional-Integral-Derivative (PID) controllers and their variants are widely preferred due to their reliable control yield and simple structure [15]. However, their limited degrees of freedom prevent them from effectively addressing the exogenous disturbances caused by changes in environmental conditions. The sliding mode controllers yield a robust control effort to extract the maximum available power while rejecting the impact of exogenous disturbances [16]. However, the switching phenomenon generates highly discontinuous control activity, which inevitably introduces chattering and harmonic distortion in the output response. Fuzzy inference systems and artificial neural networks tend to increase the flexibility of the controller design by using an elaborate set of heuristically defined qualitative rules and large training data sets, respectively [10,17]. The inaccuracies in the expert's knowledge affect the empirical definition of the fuzzy rule base, which inevitably degrades the control behavior. Furthermore, these techniques also put an excessive computational burden on the embedded processor. Adaptive neuro-fuzzy control techniques have been successfully used to implement reliable MPPT control systems [18]. The nonlinear backstepping control approaches also exhibit robust MPPT control behavior in PV systems [19]. However, despite its agility, the scheme exhibits oscillations in the system's output response. The optimal state-space and state-feedback controllers lack robustness against the model variations and parametric uncertainties caused by the rapidly changing atmospheric conditions [20].

The fractional order controllers have the innate ability to control the physical systems that exhibit chaotic and nonlinear characteristics [21]. These controllers are synthesized by integrating the control law with fractional calculus, which enables them to effectively address the emergent behavior and unmodeled intrinsic nonlinearities associated with the system being controlled [22]. The Fractional Order PID (FOPID) controllers are formulated by replacing the PID controller's integer-order differential and integral operators with fractional order counterparts [23]. The introduction of the fractional order operators adds two new parameters to the PID control law, which increase the controller's degrees of freedom and design flexibility, thus allowing it to better compensate for bounded disturbances [24]. The FOPID controllers have been extensively used to regulate the time-domain performance of power electronic energy conversion systems [25]. The FOPID control law has yielded promising results in maximum power point tracking applications [26]. However, the assignment of fixed fractional orders to the integral and differential operators tends to limit the adaptability of the MPPT control law against exogenous disturbances and environmental indeterminacies [27].

1.2. Proposed Methodology

The novel contribution of this article is the formulation of an online Adaptive FOPID (A-FOPID) compensator with self-adjusting fractional orders to extract maximum power from a stand-alone PV system as environmental conditions change. A pre-calibrated conventional FOPID compensator, which operates on the output voltage error of the interleaved buck-boost converter, is employed as the baseline maximum-power-point-tracking (MPPT) controller. The baseline controller is retrofitted with an online state-error-driven adaptation law that adaptively modulates the fractional orders of the controller's integral and differential operators. The main contributions of this article are outlined as follows:

(1) Generating the reference voltage (V_{ref}) trajectory using a pre-calibrated FNN model.
(2) Formulating a well-postulated online adaptation law using the nonlinear Hyperbolic Secant Function (HSF) of the system's state error and the error derivative variables. The waveform of the HSF is configured using well-established state-error-dependent meta-rules.
(3) Augmenting the FOPID controller with the adaptation law that dynamically self-adjusts the fractional orders of the integral and differential operators to realize the A-FOPID controller that accurately tracks the V_{ref} trajectory.
(4) Verifying the proposed controller's efficacy by carrying out customized simulations in the MATLAB/Simulink (R2022b) environment that analyze the controller's behavior under the influence of step changes in the irradiance levels and ambient temperature conditions.

The proposed scheme supplements the controller's adaptability, enabling it to manipulate flexibly the tightness of the applied control effort as the voltage error conditions change. This feature is especially beneficial in MPPT applications because it equips the control law to adapt itself in real-time as per the changes in ambient temperature and solar irradiance levels that lead to fluctuations in the MPP. The simulation results also validate that the proposed AFOPID-based MPPT control law exhibits relatively stronger damping against oscillations and a faster transient response speed against rapidly changing environmental conditions as compared to the conventional FOPID controller. The proposed control procedure is novel and has not been attempted previously for MPPT applications in the scientific literature, as per the author's knowledge.

The remaining paper is organized as follows. The PV energy system and its constituent blocks are discussed in Section 2. The proposed A-FOPID control law is formulated in Section 3. The parameter optimization scheme is described in Section 4. The simulation results and discussions are presented in Section 5. The article concludes in Section 6.

2. System Description

This section presents a description of the constituent blocks used to construct the MPPT scheme for a stand-alone PV system. The ambient temperature and solar irradiance are continuously measured via dedicated temperature sensors and radiation sensors, respectively. The measurement data is fed to the FNN block. The FNN block generates the desired reference voltage for extracting maximum power at the given atmospheric conditions. A closed-loop feedback control system is tasked with tracking the reference trajectory delivered by the FNN block. A voltage sensor is commissioned to measure the variation in the voltage across the load impedance. The control system processes the error between the measured and reference voltage levels to adjust the duty cycle of the transistor switches in the buck-boost converter. The hardware schematic diagram of the MPPT system is illustrated in Figure 1.
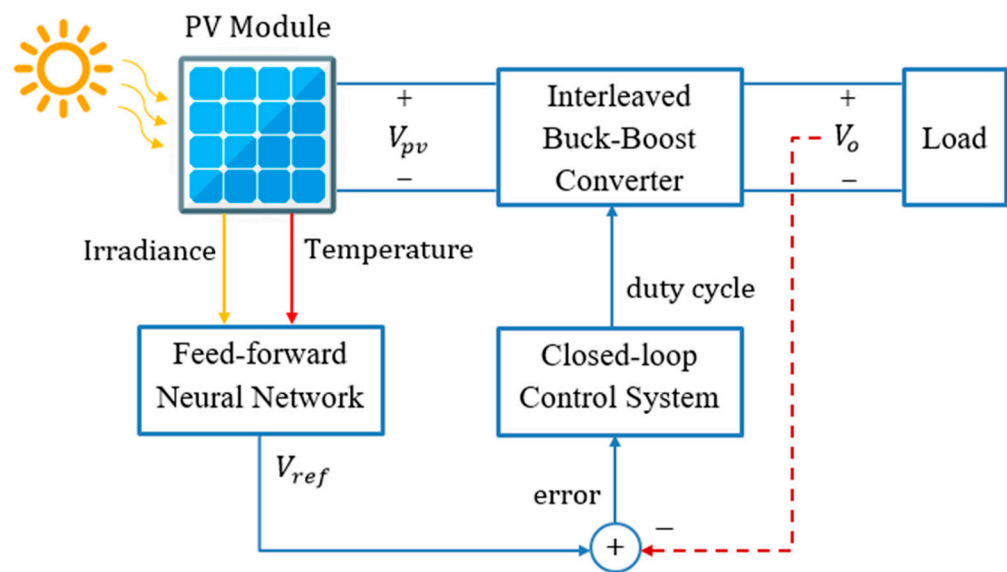
Figure 1. MPPT system's hardware schematic diagram.

2.1. Photovoltaic System Model

A PV array is fabricated via series and parallel combinations of solar cells. The PV solar cell is a p-n junction semiconductor. Hence, it can be modeled by considering the single-diode model, which is the most commonly adopted technique to model a solar cell. The equivalent circuit model of a PV solar cell is shown in Figure 2 [17]. The solar cell's output current I_{pv} is expressed as shown below [28].

$$I_{pv} = N_p I_{ph} - I_D - I_{sh} \tag{1}$$

where N_p is the number of solar cells connected in parallel, I_{ph} is the photo-current, which depends upon the ambient conditions (temperature, irradiance), I_D is the current flowing through the diode, and I_{sh} is the current flowing through the shunt resistance R_{sh}. The formulation of I_{ph} is expressed below [17].

$$I_{ph} = \frac{S}{S_{ref}} \left[I_{sc} + K_i \left(T - T_{ref} \right) \right] \tag{2}$$

where S is the solar irradiance at current condition, I_{sc} is the cell's short circuit current at reference temperature (T_{ref}) and reference irradiance (S_{ref}), K_i is the short circuit current temperature coefficient, and T is the cell's temperature. The diode current I_D is expressed as shown below [17].

$$I_D = I_{rs} N_p \left[exp \left(\frac{q \left(V_{pv} + I_{pv} R_{ser} \right)}{n K N_s T} \right) - 1 \right] \tag{3}$$

where I_{rs} is the reverse saturation current of the diode, N_s is the number of solar cells connected in series, q is the electron charge, V_{pv} is the output voltage of the solar cell, R_{ser} is the series resistance, n is the diode ideality facto, and K is the Boltzmann's constant. The expression of I_{rs} is shown below [17].

$$I_{rs} = I_{rn} \left(\frac{T}{T_{ref}} \right)^3 exp \left[\frac{E}{nK} \left(\frac{1}{T} - \frac{1}{T_{ref}} \right) \right] \tag{4}$$

where I_{rn} is the nominal reverse saturation current and E is the band-gap energy of the PV cell's semiconductor. The formulation of I_{sh} is expressed below [17].

$$I_{sh} = \frac{V_{pv} + I_{pv} R_{ser}}{R_{sh}} \tag{5}$$

where R_{sh} is the shunt resistance. The values of model parameters used for conducting the simulations in MATLAB/SIMULINK are identified in Table 1 [9,17].
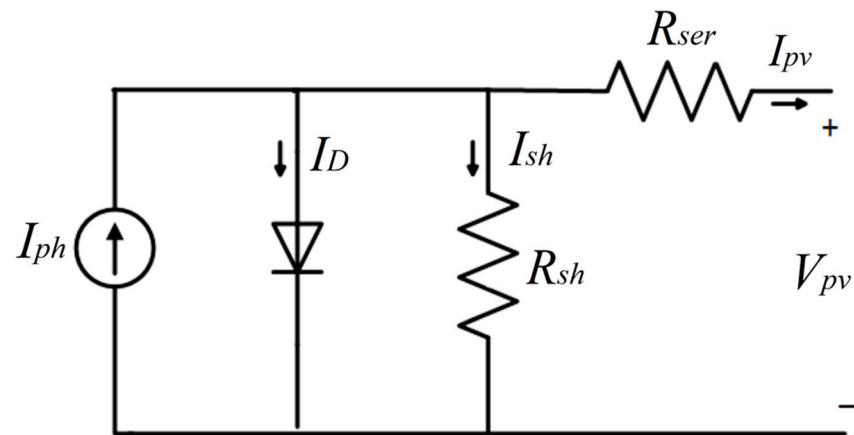

Figure 2. Single diode model of a PV module [17].

Table 1. Model parameters of the PV module [9,17].

Parameter	Value	Units
T_{ref}	298	K
S_{ref}	1000	w/m^2
I_{sc}	17.56	A
K_i	0.00479	A/°C
q	1.6×10^{-9}	C
n	1.8	-
K	1.38×10^{-23}	J/K
E	1.12	eV
R_{ser}	179.94	Ω
R_{sh}	3.17	Ω
N_s	72	-
N_p	1	-
Open circuit voltage	165.8	V
Maximum power	1555	W
Voltage at MPP	102.6	V
Current at MPP	15.16	A

2.2. Buck-Boost Converter Model

The DC-DC buck-boost converter is a power electronic circuit that is used to regulate the PV system's output voltage at a desired level [29]. It continually steps up (or steps down) the output voltage level to extract the maximum power point from the PV system [30]. To achieve the MPPT operation, the buck-boost converter minimizes the error between the output voltage (V_o) and reference voltage (V_{ref}) by appropriately modifying the duty cycle (*d*) applied to the primary switching transistor(s) of the converter circuit. The duty cycle is expressed as shown below.

$$d = \frac{t_{on}}{t_{on} + t_{off}} \tag{6}$$

where t_{on} and t_{off} represent the on-time and the off-time of the switching cycle. The duty cycle is adjusted online by employing a closed-loop negative feedback control scheme (as discussed in Section 2.3). The circuit schematic of the interleaved boost converter is shown in Figure 3 [9]. The Insulated Gate Bipolar Transistors (IGBT) switches S_1 and S_2 serve to chop down the input voltage V_{pv} into rectangular pulses. The diodes D_1 and D_2 are considered ideal. Apart from acting as charge pumps, the capacitors C_1 and C_2 are used to remove ripples from the input voltage and output voltage waveforms, respectively. The

converter is operated in continuous conduction mode and has two switching configurations, namely, switch-on configuration and switch-off configuration.
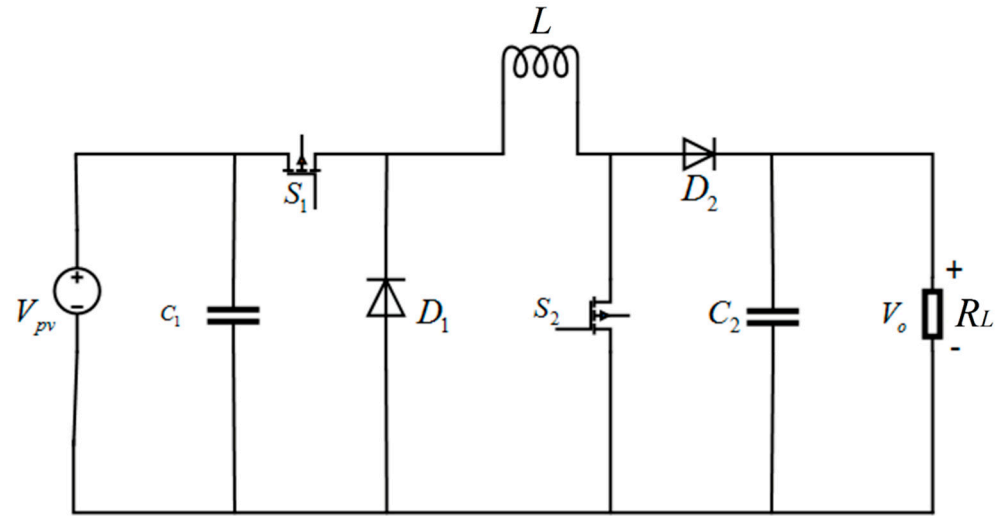

Figure 3. Buck−boost converter circuit [9].

During the switch-on configuration, the IGBT switches S_1 and S_2 are turned on. This operation puts the diodes in reverse-biased mode, which disconnects the capacitor C_2 and the load R_L from the rest of the circuit. The current I_{pv} supplied by the PV module continues to charge the inductor L, whereas the capacitor C_2 discharges itself to supply continuous current to the load. The corresponding state-space representation for the switch-on configuration is represented as follows [9].

$$\begin{bmatrix} \dot{V}_{pv} \\ \dot{I}_L \\ \dot{V}_{C2} \end{bmatrix} = \begin{bmatrix} 0 & -\frac{1}{C_1} & 0 \\ \frac{1}{L} & 0 & 0 \\ 0 & 0 & -\frac{1}{R_L C_2} \end{bmatrix} \begin{bmatrix} V_{pv} \\ I_L \\ V_{C2} \end{bmatrix} + \begin{bmatrix} \frac{I_{pv}}{C_1} \\ 0 \\ 0 \end{bmatrix} \tag{7}$$

During the switch-off configuration, the IGBT switches S_1 and S_2 are turned off. This operation puts the diodes in forward-biased mode while disconnecting the capacitor C_1 and the input supply V_{pv} from the rest of the circuit. Consequently, the charged inductor L uses the forward-biased diodes to continue supplying current to the load while charging the capacitor C_2 as well. The corresponding state-space representation for the switch-off configuration is represented as follows [9]:

$$\begin{bmatrix} \dot{V}_{pv} \\ \dot{I}_L \\ \dot{V}_{C2} \end{bmatrix} = \begin{bmatrix} 0 & 0 & 0 \\ 0 & 0 & -\frac{1}{L} \\ 0 & \frac{1}{C_1} & -\frac{1}{R_L C_2} \end{bmatrix} \begin{bmatrix} V_{pv} \\ I_L \\ V_{C2} \end{bmatrix} + \begin{bmatrix} \frac{I_{pv}}{C_1} \\ 0 \\ 0 \end{bmatrix} \tag{8}$$

The relationship between V_o, V_{pv}, and d is expressed as shown below [29].

$$V_o = \left(\frac{d}{1-d} \right) V_{pv} \tag{9}$$

The averaged state-space model of the buck-boost converter for both switching modes is shown below [9].

$$\begin{bmatrix} \dot{V}_{pv} \\ \dot{I}_L \\ \dot{V}_{C2} \end{bmatrix} = \begin{bmatrix} 0 & -\frac{d}{C_1} & 0 \\ \frac{d}{L} & 0 & -\frac{1}{L}(1-d) \\ 0 & \frac{1}{C_1}(1-d) & -\frac{1}{R_L C_2} \end{bmatrix} \begin{bmatrix} V_{pv} \\ I_L \\ V_{C2} \end{bmatrix} + \begin{bmatrix} \frac{I_{pv}}{C_1} \\ 0 \\ 0 \end{bmatrix} \tag{10}$$

In Section 2.4, the baseline FOPID control law is synthesized for dynamically adjusting the value of d to track the reference trajectory (See Section 2.3), and thus, extract maximum

power from the PV system. The model parameters of the buck-boost converter used in the MATLAB simulations are identified in Table 2.

Table 2. Model parameters of the buck-boost converter circuit [9].

Parameter	Value	Units
C_1	1.0	mF
C_2	48.0	mF
L	1.5	mH
R_L	50	Ω

2.3. Reference Voltage Generation

The reference voltage V_{ref} to be tracked by the closed-loop feedback controller for extracting maximum power from the PV system described in Sections 2.1 and 2.2 as the temperature and irradiance levels change is generated by using a two-layer FNN [31]. The FNN for V_{ref} generation is trained per PV installation separately due to their different parameter settings. The temperature and irradiance variables act as inputs to the FNN block depicted in Figure 4 [17]. The data set of the input variables used to train the FNN model is acquired by changing the temperature input between 2 °C and 75 °C intervals with a step increment of 2.0 °C, whereas the irradiance levels are varied between 600 and 1000 W/m² with a step increment of 1.0 W/m² [9]. The acquired data set is used to evaluate the inputs (or activations) a_j of the next layer by using the following rule [31].

$$a_j = \sum_{i=1}^{k} (V_{ji} p_i) + b_{jo} \tag{11}$$

where p_i is the input of node i, V_{ji} is the scalar weight, b_{jo} is the reconstruction error (or bias), $k = 2$ is the total number of input variables, and $j = 1, 2, 3, \ldots, l_o$ is the number of neurons existing in the hidden layer. In this work, 10 neurons are used in the hidden layer [31]. The activation of each layer is computed by using a Hyperbolic Tangent Function (HTF) that depends on a_j. The HTF is employed because it is odd-symmetric, smooth, and bounded between -1 and 1. The output of the activation function at each hidden layer is expressed as shown below.
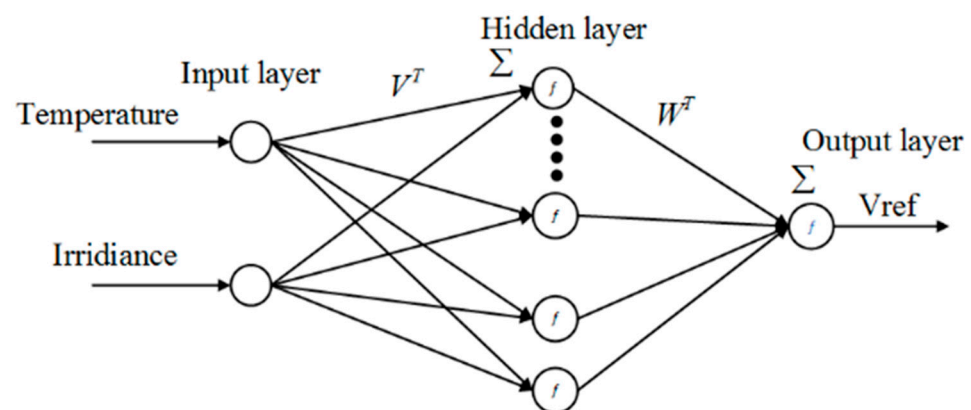
$$y_i = f(a_j) \tag{12}$$

Figure 4. FNN block for reference voltage generation [17].

The variable y_i is used in the computation of the activation of the next layer. The total activation of the output layer delivers the updated value of V_{ref}. The net activation is evaluated as expressed in (13).

$$V_{ref} = \sum_{j=1}^{l_o} (w_j y_i) + b_{ko} \tag{13}$$

where y_i serves as the input from the hidden layer upon which the HTF activation is applied, w_j represents the scalar weight between the jth hidden layer node and the output layer node, b_{ko} is the bias. By substituting the expression of y_i in (13), the expression of V_{ref} is modified as shown below.

$$V_{ref} = \sum_{j=1}^{l_o} \left(w_j f \left(\sum_{i=1}^{n} (V_{ji} p_i) + b_{jo} \right) \right) + b_{ko} \tag{14}$$

The expression above can be rewritten in vector form, as shown below [9].

$$V_{ref} = W^T \hat{f} \left(V^T \hat{p} + b_v \right) + b_w \tag{15}$$

where W^T and V^T represent the weights between the layers in their respective vector form. The final expression used to compute V_{ref} is simplified as expressed in (16), [9].

$$V_{ref} = W^T \tanh \left(V^T \hat{p} + b_v \right) + b_w \tag{16}$$

where $\tanh(.)$ represents the HTF. For a given temperature and irradiance level, the characteristic curve of the PV module delivers a maximum voltage level.

This voltage level is targeted as the desired V_{ref} by the FNN model during the training phase. The network is trained by minimizing the following cost function that computes the Mean Squared Error (MSE) between the target and actual network outputs [17].

$$J \left(V_{ji}, w_j \right) = \frac{1}{2} \sum_{i=1}^{l_o} (t - z)^2 \tag{17}$$

where t is the target output and z is the actual output observed at the output node. The Levenberg-Marquardt algorithm is used to dynamically modify the weights after every iteration in the FNN model during the training phase [9,17]. The three-dimensional V_{ref} trajectory for various values of irradiance and temperature levels generated by the FNN is depicted in Figure 5. The MSE is used to ascertain the training progress of the FNN. The global minimum value of the MSE (1.0836×10^{-6}) occurs at 1000 epochs (See [9]). The regression graph and the estimation error histograms associated with V_{ref}, as illustrated in [9], also validate that the data generated by FNN closely resembles the target data.
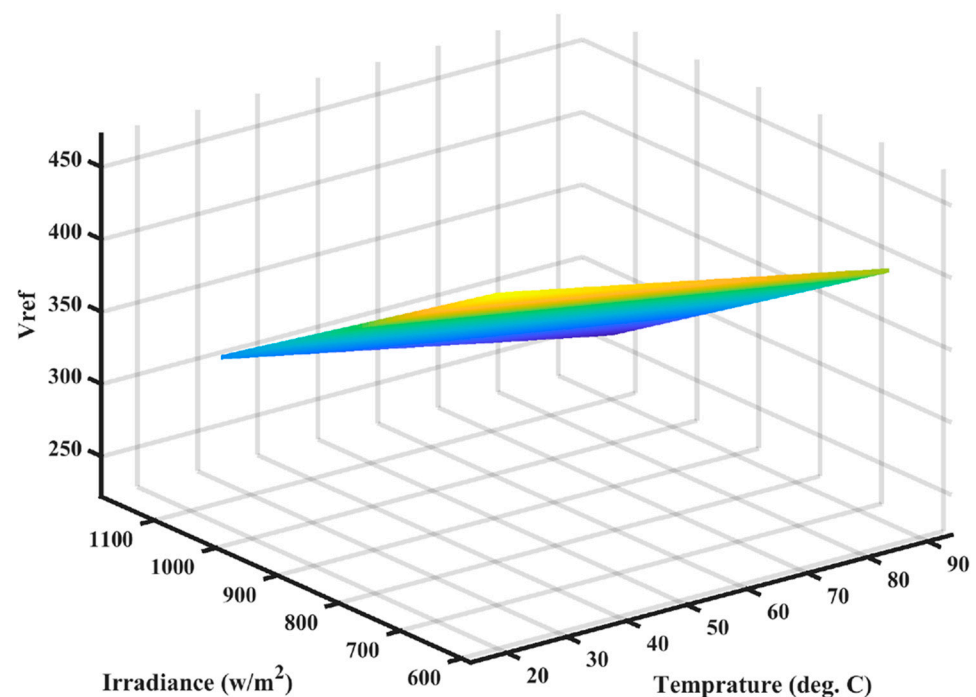

Figure 5. FNN model used for reference generation [17].

2.4. Fractional Order PID Control Law

The V_{ref} generated by the FNN block is tracked by a closed-loop FOPID controller to extract the maximum from the PV system under every atmospheric condition. The FOPID control procedure is devised by augmenting an integer-order PID controller with fractional order operators. The integer-order PID control law is formulated as the linear combination of the system's classical error, integral of error, and derivative of error [15]. The proportional control factor minimizes the instantaneous error, the integral control factor minimizes the steady-state oscillations while tracking the reference trajectory, and the derivative control factor increases the system's transient recovery response speed. The integer-order PID voltage regulator is formulated as shown below [15].

$$d(t) = k_p e(t) + k_i \int_0^t e(\tau)d\tau + k_d \dot{e}(t) \tag{18}$$

where $e(t) = V_{ref} - V_o(t)$. $e(t)$ represents the error between the reference and the actual voltage levels at the converter's output, k_p is the proportional gain, k_i is the integral gain, and k_d is the differential gain. The value of $d(t)$ is normalized between 0 and 1 to ensure that the duty cycle applied to the IGBT switches is bounded between 0 and 100% under every operating condition.

To enhance the controller's design flexibility and disturbance rejection ability, the integer-order PID control law is transformed into the FOPID control law simply by assigning pre-configured fractional orders (powers) to the integral and differential operators of the original control law [23]. The proposed augmentation introduces two additional parameters in the control law, which increase its degrees of freedom to effectively reject the exogenous perturbations caused by environmental uncertainties [25,26]. The fractional order operators are symbolically represented as Q^λ; where, λ represents the value of the fractional order. The fractional operators are mathematically represented by the following well-known definitions offered by Riemann-Liouville, Gruunwald-Letnikov, and Caputo [32].

$$Q^\lambda f(t) = \frac{1}{\Gamma(n-\lambda)} \frac{d^m}{dt^m} \int_a^t \frac{f(\tau)}{(t-\tau)^{\lambda-m+1}} d\tau \tag{19}$$

where $\Gamma(x)$ is the Euler gamma function, m is an integer such that $m-1 < \lambda < m$.

$$Q^\lambda f(t) = \lim_{h \to 0} \frac{1}{h^i} \sum_{i=0}^{(t-a)/h} (-1)^i \binom{\lambda}{i} f(t-ih) \tag{20}$$

where $\binom{\lambda}{i} = \Gamma(\lambda+1)/\Gamma(i+1)\Gamma(\lambda-i+1)$, and h is the step size.

$$Q^\lambda f(t) = \frac{1}{\Gamma(\lambda-m)} \int_a^t \frac{f^m(\tau)}{(t-\tau)^{\lambda-m+1}} d\tau \tag{21}$$

The FOPID controller is thus formulated by replacing the integer-order integral and differential operators with their fractional order counterparts, as shown below [23,24].

$$d(t) = k_p e(t) + k_i \left(Q^{-\alpha} e(t) \right) + k_d \left(Q^\gamma e(t) \right) \tag{22}$$

where α and γ are the fractional orders assigned to the integral and differential operators, respectively. The values of these two fractional orders are bounded between 0 and 1. The integer order differential operator is replaced with $Q^\gamma e(t)$ and integer order integral operator is replaced with $Q^{-\alpha} e(t)$. Together with the existing PID gains, the fractional control law is now equipped with five distinct parameters (k_p, k_i, k_d, α, and γ) that increase the controller's degrees of freedom to effectively manipulate the applied control effort and minimize the state deviations. The block diagram of the FOPID control system is depicted in Figure 6. The transfer function of the FOPID control law is expressed as shown below.

$$C(s) = \frac{D(s)}{E(s)} = k_p + \frac{k_i}{s^\alpha} + k_d s^\gamma \tag{23}$$

where, s represents the Laplace operator. Owing to their fractional nature, the computational implementation of the terms s^γ and s^α is quite difficult. However, in this research work, the aforementioned fractional order terms are approximated via the Oustaloup recursive filters [21]. The Oustaloup approximation technique used to realize the fractional terms is shown below [22].

$$s^\lambda = \prod_{i=1}^{P} \frac{1 + \left(\frac{s}{v_{z,i}}\right)}{1 + \left(\frac{s}{v_{p,i}}\right)} \tag{24}$$

such that, $v_{z,i} = v_L \left(\frac{v_H}{v_L}\right)^{\frac{2i-1-\lambda}{2M}}, v_{p,i} = v_L \left(\frac{v_H}{v_L}\right)^{\frac{2i-1+\lambda}{2M}}$. P is the filter's order, and v_L and v_H represent the filter's lower and upper translational frequencies, respectively. In this research, a 5th-order Oustaloup's filter is utilized with $v_L = 10^{-3}$ rad/s and $v_H = 10^2$ rad/s to approximate the said fractional terms. The stability and robustness of the designed FOPID controller are analyzed as per the basic definitions of the gain margin and phase margin in the frequency domain. The feedback control system is required to satisfy the following conditions to ensure its stability [33].
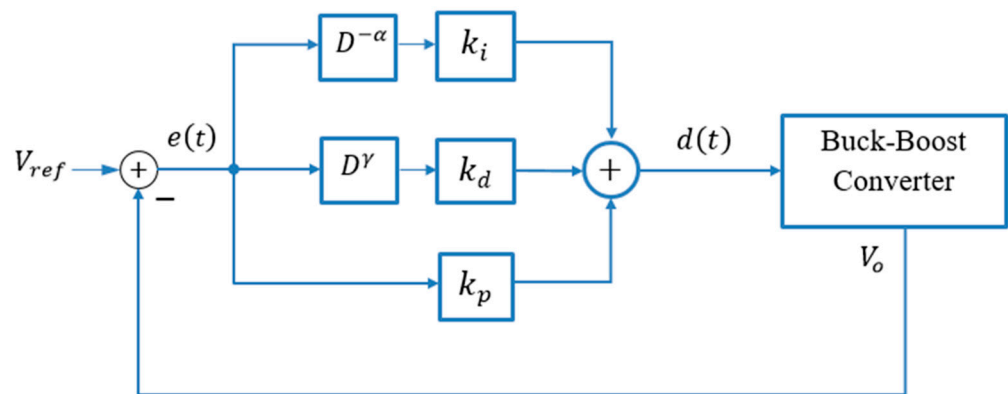

Figure 6. Block diagram of the FOPID control system.

- The open loop system's phase at the gain cross-over frequency ω_o must satisfy: $arg(C(j\omega_o)G(j\omega_o)) = \varphi_m - \pi$, where φ_m is the phase margin and $G(.)$ is the system's overall transfer function that is derived using (10).
- The open loop system's gain at ω_o must satisfy: $|C(j\omega_o)G(j\omega_o)| = 0\ dB$.
- To uphold robustness against loop-gain changes, the phase must satisfy: $\frac{d}{d\omega}[arg(C(j\omega)G(j\omega))]|_{\omega=\omega_o} = 0$.
- To reject high-frequency noise $\omega \geq v_h$, the closed-loop transfer function Q must satisfy: $\left|Q(jv_h) = \frac{C(jv_h)G(jv_h)}{1+C(jv_h)G(jv_h)}\right| < H\ dB$.
- To reject low-frequency noise $\omega \leq v_l$, the sensitivity function S must satisfy: $\left|S(jv_l) = \frac{1}{1+C(jv_l)G(jv_l)}\right| \leq M\ dB$.

In this research, the following specifications are considered; $\varphi_m = 0.785\ rad.$, $\omega_c = 0.5$, $H = -10$, and $M = -20$. These settings are decided as per the expert's experience. The aforementioned specifications are satisfied while computing the five parameters of the FOPID controller to preserve its asymptotic stability. The FOPID controller parameters are tuned via the optimization technique discussed in Section 4.

3. Proposed Adaptive FOPID Control Scheme

The fixed values of FOPID controller parameters incapacitate the control law to robustly compensate for parametric uncertainties and environmental perturbations. Selecting

an optimal set of k_p, k_i, k_d, α, and γ that yields robust control effort under every operating condition is quite difficult. Due to its inherent design limitations, the fixed values of fractional orders render the FOPID control procedure wasteful by contributing insufficient control resources under transient disturbances and superfluous control resources under steady-state conditions, especially for the PV system that encounters abrupt state variations.

For a given error condition, an appropriate setting of α and γ can transform the proposed FOPID control law into an integer order P, PI, PD, or PID controller, as shown in Table 3 [26]. Each of the aforementioned integer-order controller subclasses is beneficial for effectively addressing a specific phase of the system's state response. For example, the applied integral control effort should be mild, while the derivative control effort should be enhanced during the transient disturbances and initial start-up to dampen the overshoots and ensure faster transient recovery. Conversely, the applied integral control effort should be stiffer while the derivative control effort should be softer as the response converges to steady state to ensure smooth settlement with minimal fluctuations. The aforementioned arrangement can be realized by adaptively modulating the values of α and γ via an online state-error-driven adaptation scheme that allows for a smooth commutation of the fractional orders between 0 and 1 [26].

Table 3. Generalization of the FOPID controller.

α	γ	Controller
0	0	P
0	1	PD
1	0	PI
1	1	PID

This scheme obviates the necessity of individually pre-calibrating the values of α and γ offline. The proposed adaptation strategy used is formulated as per the following state-error-dependent meta-rules.

During the transient phase, the response becomes farther from the reference voltage. In this situation, the value of α is reduced while γ is enlarged to strengthen the derivative control action and increase the transient response speed.

As the response converges to the reference, the value of α is progressively increased while γ is reduced to strengthen the integral control action, effectively damping the overshoots (and oscillations) while gently settling the response at the reference.

The aforementioned rationale aids in significantly minimizing the trajectory tracking errors by adaptively manipulating the controller's response speed during transient conditions as well as its damping control effort as the response settles. The proposed adaptation scheme is practically realized by using a pre-calibrated HSF that depends on the weighted sum of the error $e(t)$ and its derivative $\dot{e}(t)$.

The HSF is chosen because its waveform is smooth, which ensures a smooth transition of the parameters, it can be bounded between 0 and 1, and it is even symmetric [34]. All of these characteristics comply with the aforementioned meta-rules. The time-varying functions used to online self-adapt the fractional orders α and γ are formulated in (25).

$$\alpha(t) = \operatorname{sech}(z(t)), \;\; \gamma(t) = 1 - \alpha(t) \tag{25}$$

Such that $z(t) = \beta\, e(t) + \delta\, \dot{e}(t)$. $\operatorname{sech}(.)$ represents the HSF, and β and δ are preconfigured positive constants that determine the variation rate of the HSF. The values of β and δ are optimized by using the tuning procedure suggested in Section 4. Together, these two parameters configure the shape and form of the HSFs. The weighted sum of $e(t)$ and $\dot{e}(t)$ delivers the compounded error variable $z(t)$ that accurately informs the systems regarding the phase of the state response. Thus, when the response is farther from the desired reference, the aforesaid compounded-error variable automatically enlarges, as shown in Figure 7, to inflate γ and reduce α by using the adaptation functions given in (25). Similarly, when the response converges to the desired reference, the magnitude of

the compounded error reduces, as shown in Figure 7, to reduce γ and increase α. This arrangement fully complies with the aforementioned rules. With the augmentation of the self-adjusting fractional orders, the resulting Adaptive-FOPID (A-FOPID) control law is expressed in (26).

$$d(t) = k_p e(t) + k_i \left(Q^{-\alpha(t)} e(t) \right) + k_d \left(Q^{\gamma(t)} e(t) \right) \tag{26}$$
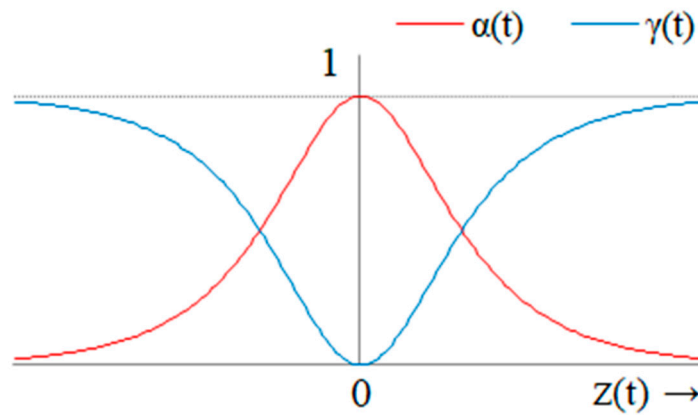

Figure 7. Waveform of the HSFs used to self-adjust the fractional orders.

The values of k_p, k_i, and k_d for the A-FOPID control law are re-calibrated by using the tuning procedure discussed in Section 4. The functions $\alpha(t)$ and $\gamma(t)$ can be easily programmed in the simulation software. These algebraic equations can be solved in a single step after every sampling instant, and thus, do not put any recursive computational burden on the digital computer. The stability criteria prescribed in Section 2.4 are sufficient to uphold the stability of the A-FOPID control law as well. The A-FOPID control block diagram is depicted in Figure 8.
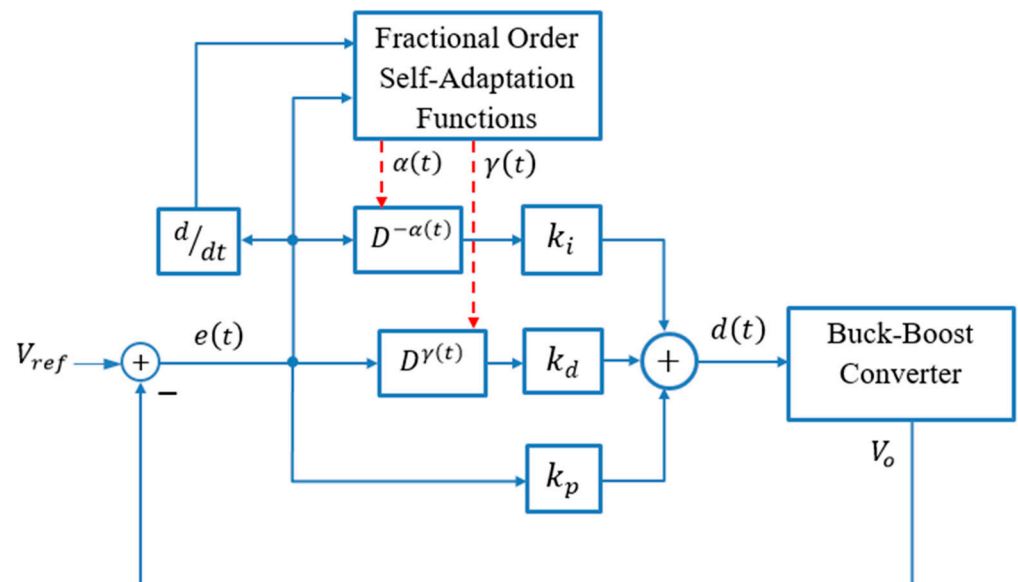

Figure 8. Block diagram of the proposed A-FOPID control system.

4. Parameter Tuning Procedure

As mentioned earlier, selecting an optimal set of k_p, k_i, k_d, α, and γ that yields optimal control effort under every operating condition is quite difficult. The manual selection of the controller parameters is limited by the expert's knowledge and, thus, may yield

inaccurate settings. Hence, in this work, the following objective function is used to tune the controller parameters.

$$J = \int_0^T \left(|e(\tau)|^2 + |d(\tau)|^2 \right) d\tau \tag{27}$$

The flow chart of the parameter tuning algorithm is illustrated in Figure 9. The parameters are tuned after repeating the simulations. The offline selection process is initiated by picking a random set of controller parameters (PID gains and fractional/complex orders) from the pre-defined search space (See Table 3). In every simulation trial, the controller parameters are heuristically updated, and the closed-loop system is allowed to regulate the output voltage at 400 V DC from an initial state of 0 V for 1 min. The corresponding cost J_n for that trial is evaluated; where, n is the trial number. The range space is searched in the direction of the steepest gradient descent of J [35]. If the cost of the present trial (J_n) is found to be less than the cost of the previous trial (J_{n-1}), the local minimum-cost variable J_{min} is modified. This arrangement ensures that the exploration continues to progress in the direction of the objective function's negative gradient, thus ensuring its minimization. The exploration for the optimum parameter values is concluded if either J_{min} acquires a predefined threshold cost or the algorithm has completed the maximum number of trials (n_{max}) allowed. Based on the designer's experience, the threshold value for J_{min} is predetermined at 1×10^5 and n_{max} is preset at 30 in this work. Finally, the obtained parameter values are refined by manually fine-tuning them to satisfy the stability specifications prescribed in Section 2.4. The tuned parameter values are shown in Table 4.
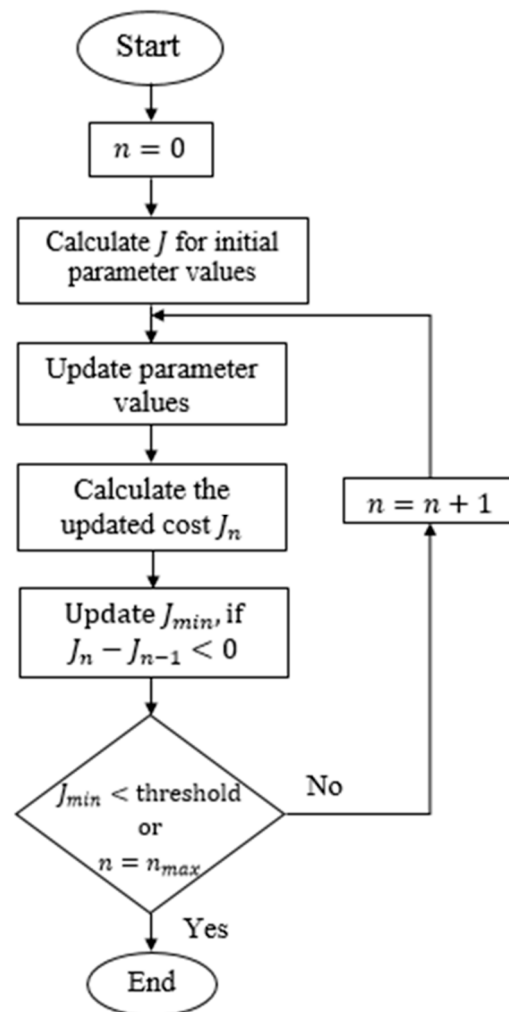

Figure 9. Flow chart of the parameter tuning algorithm.

Table 4. Optimized controller parameters.

Parameters	Selection Range	Initial Value	Optimized Values	
			FOPID	**A-FOPID**
k_p	[0, 0.1]	1×10^{-2}	0.432	0.427
k_i	[0, 0.1]	1×10^{-2}	0.106	0.112
k_d	[0, 0.1]	1×10^{-2}	0.028	0.034
α	[0, 1]	0.1	0.84	-
γ	[0, 1]	0.1	0.66	-
β	[0, 1]	0.01	-	0.095
δ	[0, 1]	0.01	-	0.028

5. Simulation Results and Discussions

This section presents the details of the customized simulations and the comprehensive analysis of the obtained results.

5.1. Simulation Setup

The MPPT performance of the FOPID and A-FOPID control laws under the influence of step changes in solar irradiance levels and temperature conditions are assessed via customized simulations that are performed using MATLAB/Simulink (R2022b) software [36]. The software is operated on a personal computer that is equipped with a Core i7, 64-bit, 2.1 GHz CPU, and 8.0 GB of RAM.

The fractional integral and differential operators are realized via the built-in functions provided by MATLAB's FOMCON toolbox. The sampling frequency of the simulation is set at 1.0 kHz. The model parameters of the PV module and the buck-boost converter, identified in Tables 1 and 2, respectively, are used to carry out the simulations. The control input signal $d(t)$ is restricted between 0 and 1 via a saturation function to safely operate the IGBT switches of the buck-boost converter.

5.2. Simulations and Results

The effectiveness of the FOPID and A-FOPID controllers to accurately track the reference trajectory for extracting maximum power under every operating condition is analyzed by introducing step changes in the irradiance levels and ambient temperature at regular intervals. The impact of these environmental disturbances is analyzed via the two test cases described below. A simulated white Gaussian noise signal is also injected in $d(t)$ to emulate the effects of measurement noise contributed by the output voltage sensor, radiation sensor, and temperature sensor in the MPPT response.

A. *Reference tracking under varying irradiance*: This simulation examines the capability of the FOPID and A-FOPID control laws to extract maximum power under varying irradiance levels. In this test case, step changes are introduced in the irradiance levels at regular intervals, as shown in Figure 10, while the temperature is kept constant at 25 °C (298 K). The designed controllers are tasked with tracking the V_{ref} trajectory generated by the FNN scheme for the varying irradiance profiles. The resulting reference voltage trajectory tracking behavior and MPPT profile of the PV array are shown in Figures 11 and 12, respectively. The results show that the A-FOPID achieves the MPP without any significant overshoots and with a faster response speed. It also minimizes the steady-state fluctuations in the response. Whereas the FOPID controller exhibits a relatively slower response speed with persistent oscillations (and chattering) in the response. The results validate the superior robustness and reference tracking accuracy of the A-FOPID controller.

B. *Reference tracking under varying ambient temperatures*: This simulation examines the controller's ability to extract maximum power under varying outdoor temperature levels. The temperature levels are varied as shown in Figure 13, while the irradiance is kept constant at 1000 W/m². The controllers track the reference trajectory for the varying temperature profiles. The reference voltage and the MPP tracking profiles

are shown in Figures 14 and 15, respectively. The results show that the A-FOPID controller achieves the MPP with better accuracy, a faster response speed, and minimal oscillations. The FOPID controller exhibits a relatively slower response speed with oscillations. The results validate the enhanced reference tracking behavior of the A-FOPID controller.
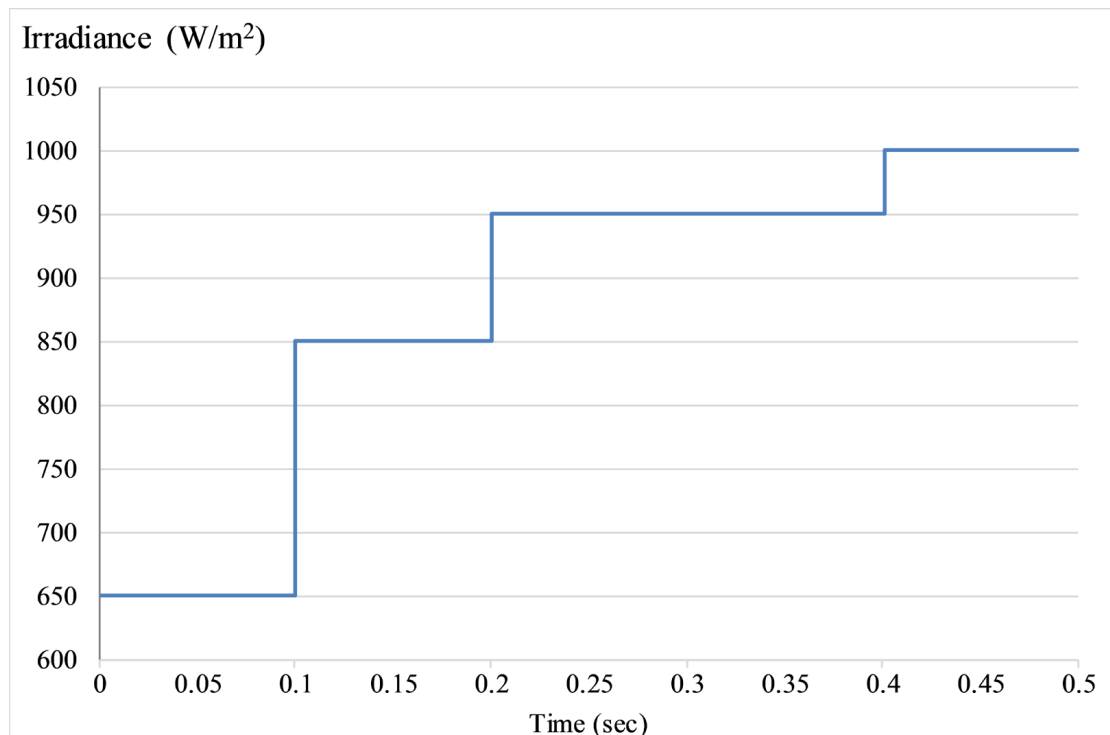

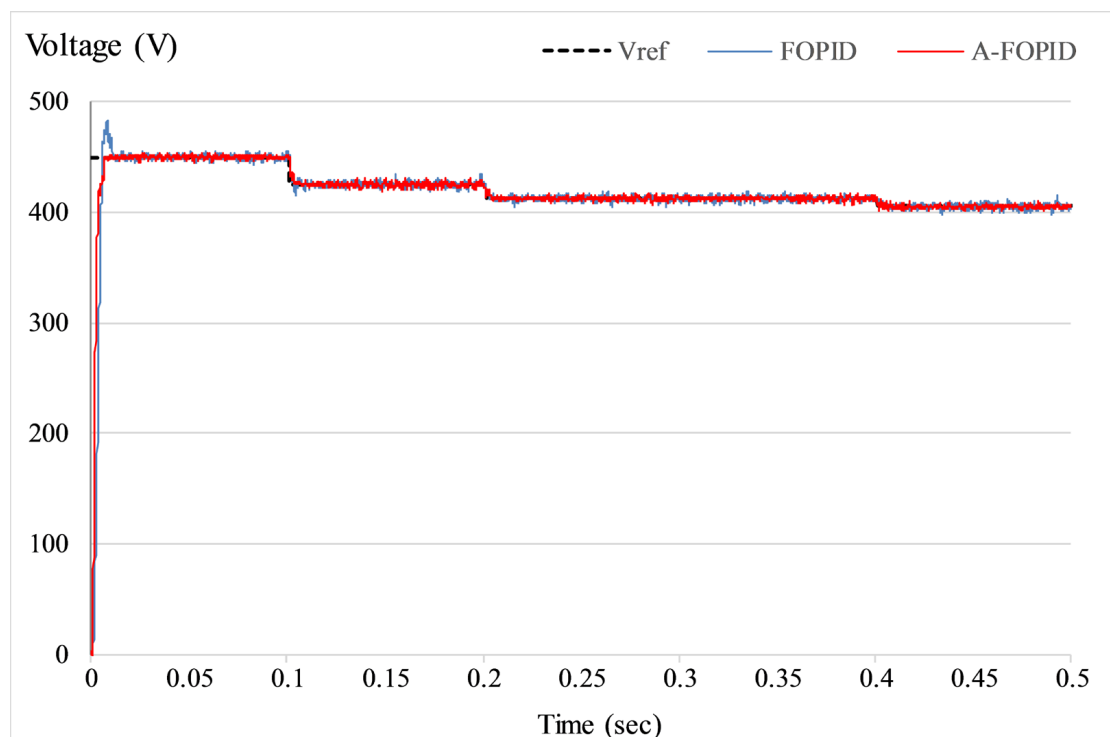**Figure 10.** Step changes in the solar irradiance levels.

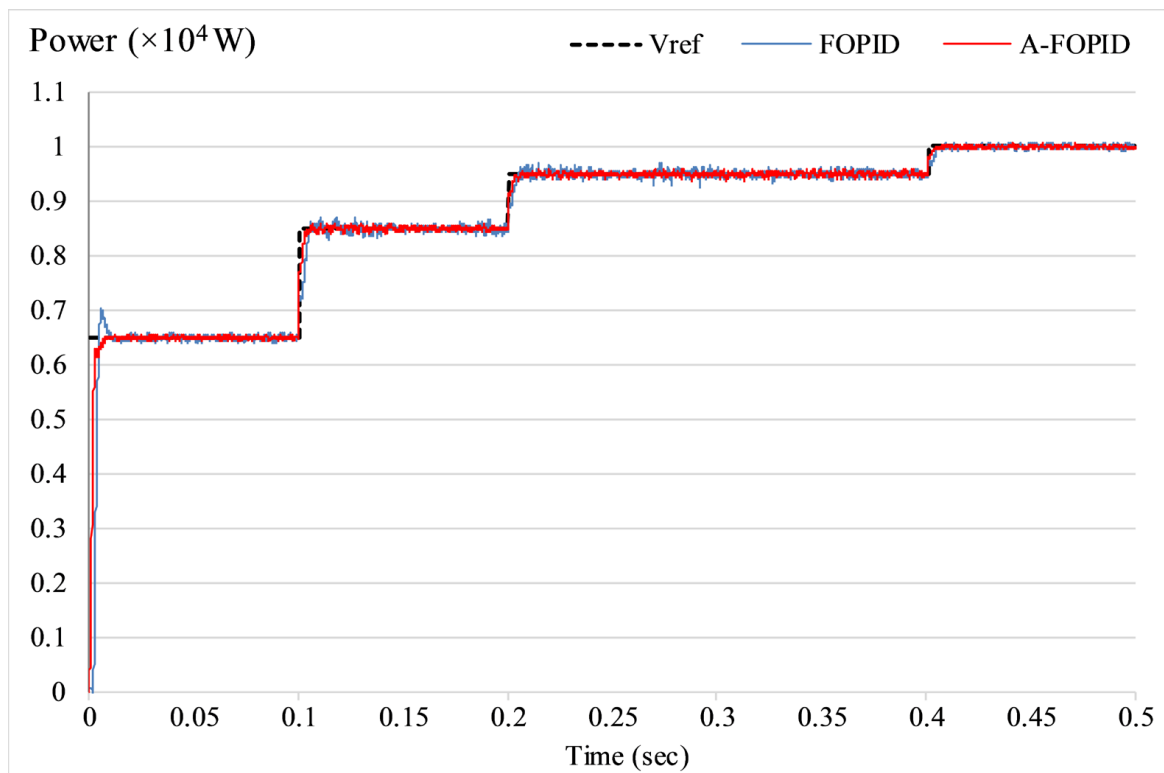**Figure 11.** Reference voltage tracking behavior under varying irradiance.

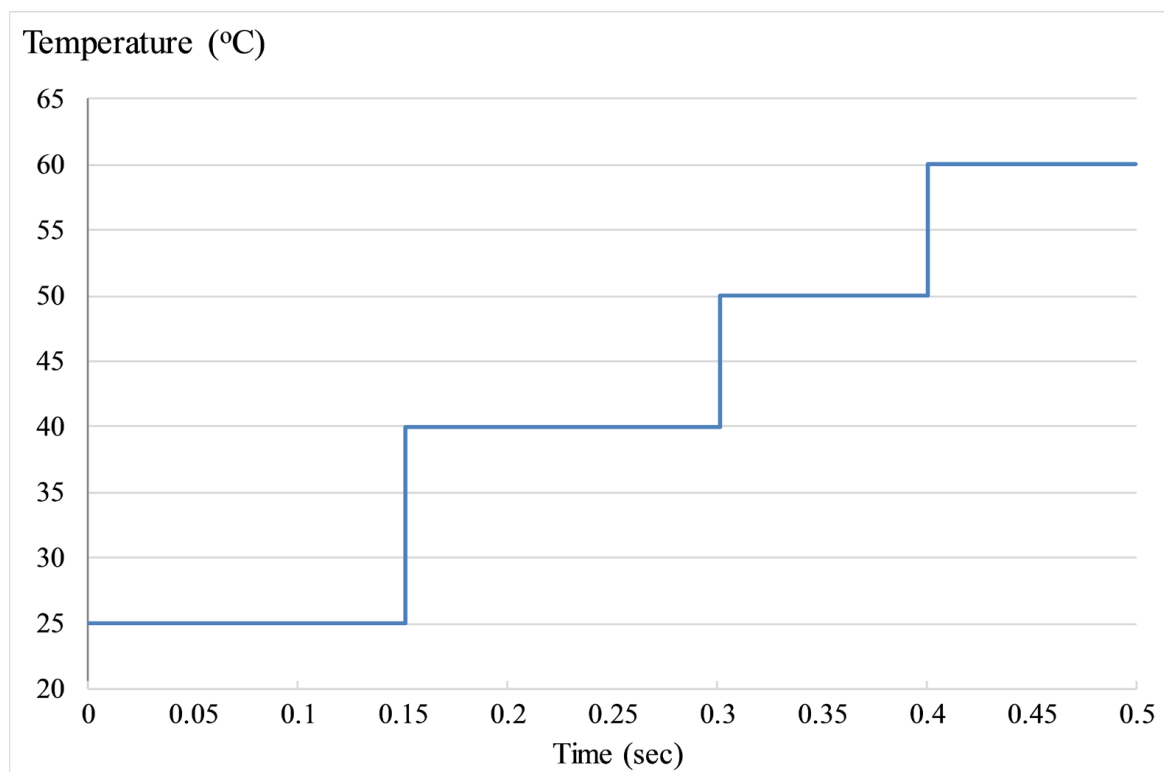**Figure 12.** MPPT profile under varying irradiance.

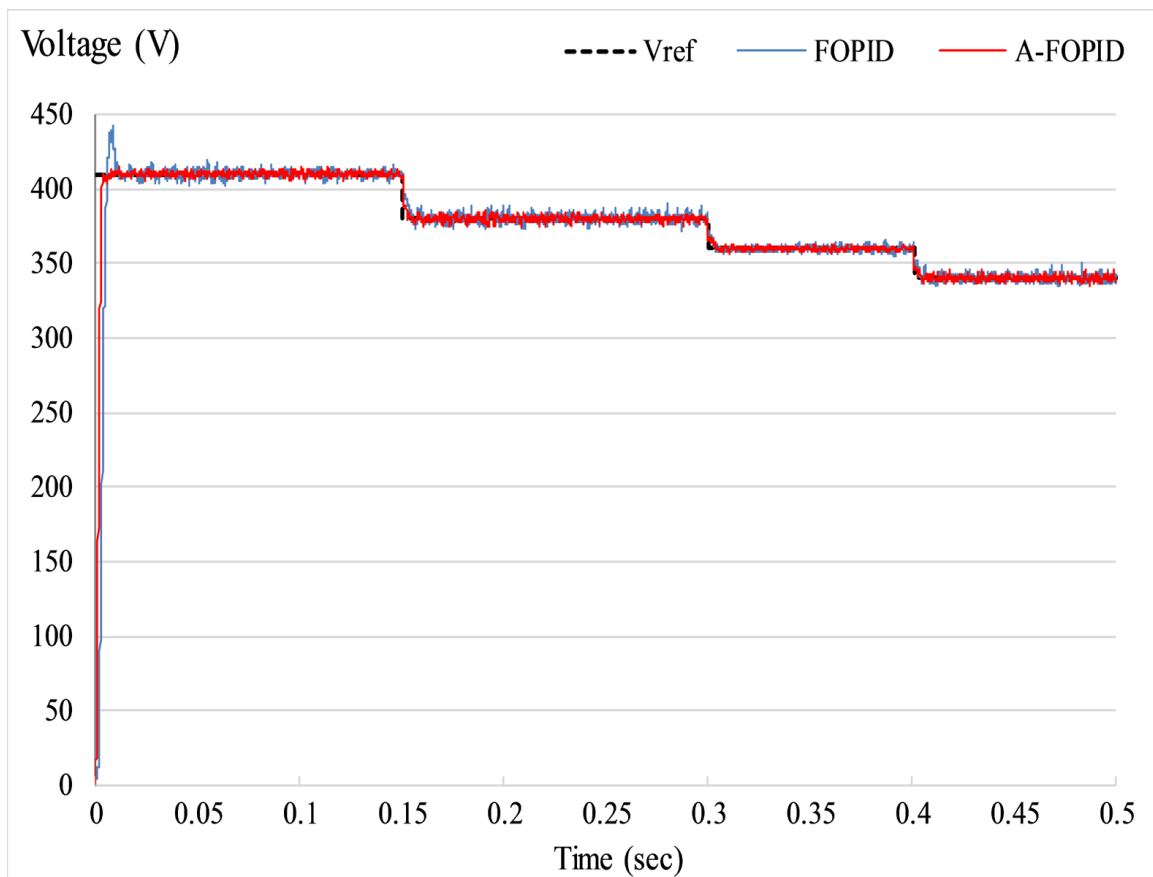**Figure 13.** Step changes in the outdoor temperature levels.

Figure 14. Reference voltage tracking behavior under varying temperatures.
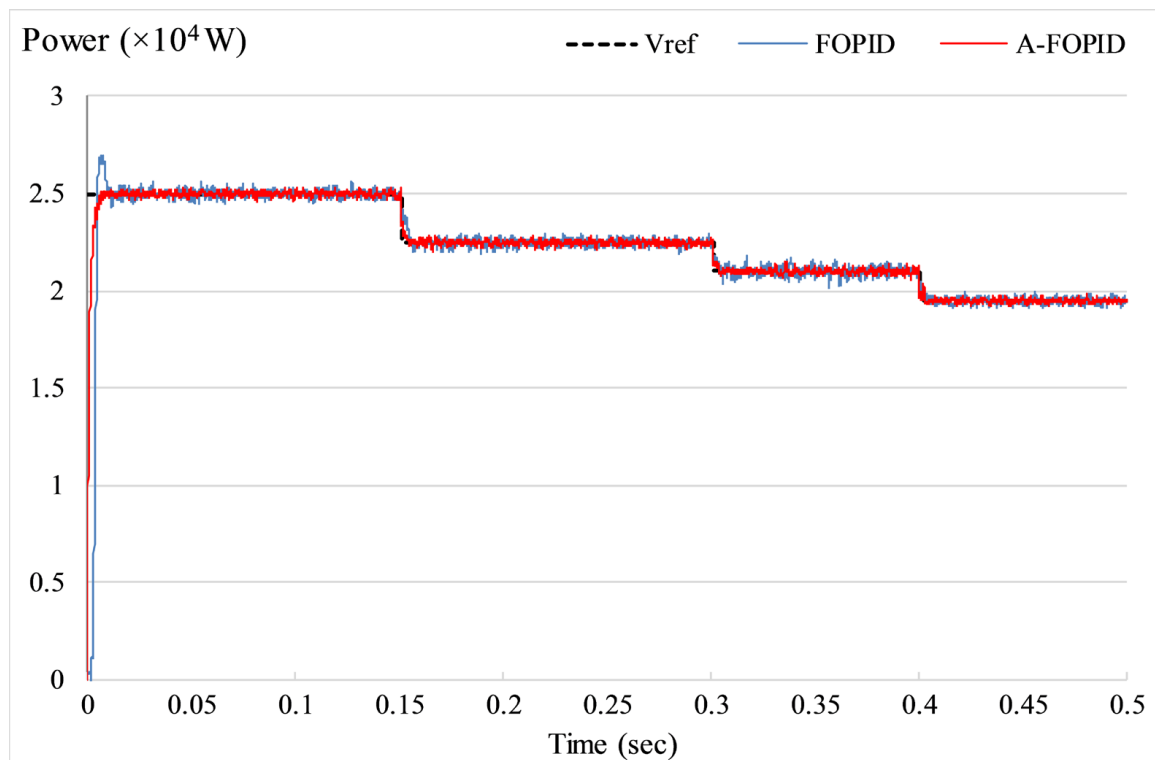

Figure 15. MPPT profile under varying temperatures.

5.3. Analytical Discussions

The simulation results are quantitatively analyzed by utilizing the following critical performance indicators.

- V_{RMSE}: Root-mean-squared value of error, $e(t)$.
- OS: Overshoot in V_o after the initial start-up.
- T_{set}: Time taken by the signal to settle at the desired voltage after initial start-up.
- P_{RMSE}: Root-mean-squared value of the error in the output power levels of the PV array.

These performance indicators ascertain the time optimality and reference tracking accuracy of each control procedure designed here. The simulation results are summarized in Table 5. The simulation results verify the superior time optimality and reference tracking accuracy of the A-FOPID controller as compared to the FOPID controllers. The enhancement in the transient recovery behavior and minimization of the reference tracking errors demonstrated by the A-FOPID controllers is attributed to the assignment of the self-adjusting fractional orders to the integral and differential operators of the control law. The error-phase-driven expert system significantly improves the self-reasoning capability of the adaptation law and enables it to execute flexible online dynamic adjustment of the fractional orders. This arrangement improves the adaptability of the control law and strengthens its disturbance compensation capability.

Table 5. Optimized controller parameters.

Simulation	Performance Indicator		Controller		Performance Improvement
	Metric	**Unit**	**FOPID**	**A-FOPID**	
A	V_{RMSE}	V	35.05	27.28	22.2%
	OS	V	25.35	3.38	86.7%
	T_{set}	sec	0.014	0.012	14.3%
	P_{RMSE}	kW	5.15	3.21	37.7%
B	V_{RMSE}	V	27.50	19.63	28.6%
	OS	V	30.61	4.88	84.0%
	T_{set}	sec	0.012	0.011	8.3%
	P_{RMSE}	kW	1.77	0.92	48.0%

It is to be noted that this study does not investigate the impact of moss, sand, or dust covering the PV array [37]. The proposed closed-loop scheme is also not particularly designed to address the effects of partial shading conditions [38]. Instead of considering different irradiance levels on the PV array caused by non-uniform shading, the FNN model used in this work is limited to generating the V_{ref} based on a singular irradiance level that is uniformly distributed across the entire PV array. This research work focuses on enhancing the controller's robustness against uniformly varying temperature and irradiance levels while extracting maximum power from a given PV capacity.

6. Conclusions

The PV system is an efficient and pollution-free renewable energy system that can fulfill the ever-increasing global energy demands. However, its output power vernation is affected by the real-time variations in the solar irradiance and the outdoor temperature conditions. Hence, MPPT controllers are adopted to extract maximum power from the PV system under varying atmospheric conditions. The reference voltage trajectory is generated by using the FNN scheme. This article systematically develops and validates the effectiveness of a robust A-FOPID controller that tracks the reference trajectory. The proposed control law is synthesized by augmenting the baseline FOPID controller with self-adjusting fraction orders of the integral and differential operators by using an online adaptation law. The adaptation law is formulated as nonlinear HSFs that depend on the magnitudes of the voltage error and its derivative. The waveforms of the adaptation functions are calibrated as per the state-error-driven meta-rules. The A-FOPID control

law significantly improves the reference tracking accuracy and time optimality of the MPPT scheme to continue extracting maximum power under rapidly varying atmospheric conditions. These propositions are justified by conducting credible simulations in the MATLAB Simulink environment. The simulation results show that the A-FOPID controller yields a mean improvement of 25.4% in tracking accuracy and 11.3% in transient response speed under varying environmental conditions. The proposed scheme is computationally economical and can be easily realized using modern digital computers. Moreover, it is highly scalable and can be extended to other alternative energy conversion systems as well. In the future, the efficacy of the proposed A-FOPID control law can be investigated by conducting hardware-in-loop experiments on a solar PV system. Intelligent expert systems and soft computing techniques can be employed to further increase the robustness of the online adaptation mechanism. The proposed A-FOPID control law can be modified and applied to wind energy conversion systems as well to assess its scalability. The complex-order PID control laws can also be investigated to improve the MPPT scheme for PV systems. Finally, the FNN model can be appropriately modified and trained to generate the global-best reference voltage when the PV system is subjected to different irradiance levels (at different locations on the module) to address the effects of partial shading conditions as well as the accumulation of moss, dust, or sand on the PV arrays.

Author Contributions: Conceptualization, O.S.; methodology, O.S. and S.A.; software, O.S. and S.A.; validation, J.I.; formal analysis, O.S.; investigation, O.S. and S.A.; resources, J.I.; data curation, S.A.; writing—original draft preparation, O.S.; writing—review and editing, J.I.; visualization, O.S. and J.I.; supervision, J.I.; project administration, J.I. All authors have read and agreed to the published version of the manuscript.

Data Availability Statement: The authors declare that the data analyzed during this study to support the findings will be made available on reasonable request.

Conflicts of Interest: The authors declare no conflict of interest.

References

1. Irfan, M.; Iqbal, J.; Iqbal, A.; Iqbal, Z.; Riaz, R.A.; Mehmood, A. Opportunities and challenges in the control of smart grids-Pakistani perspective. *Renew. Sustain. Energy Rev.* **2017**, *71*, 652–674. [CrossRef]
2. Mohamed, M.A.; Eltamaly, A.M.; Alolah, A.L. PSO-based smart grid application for sizing and optimization of hybrid renewable energy systems. *PLoS ONE* **2016**, *11*, e0159702. [CrossRef] [PubMed]
3. Iqbal, J.; Khan, Z.H. The potential role of renewable energy sources in robot's power system: A case study of Pakistan. *Renew. Sustain. Energy Rev.* **2017**, *75*, 106–122. [CrossRef]
4. Hassan, M.U.; Nawaz, M.I.; Iqbal, J. Towards autonomous cleaning of photovoltaic modules: Design and realization of a robotic cleaner. In Proceedings of the IEEE International Conference on Latest trends in Electrical Engineering & Computing Technologies, Karachi, Pakistan, 15–16 November 2017.
5. Zhou, S.; Kang, L.; Sun, J.; Guo, G.; Cheng, B.; Cao, B.; Tang, Y. A novel maximum power point tracking algorithms for standalone photovoltaic system. *Int. J. Control Autom. Syst.* **2011**, *8*, 1364–1371. [CrossRef]
6. Pandya, R.; Vardia, M. Grid-connected PV system with MPPT control and P&O technique. *Int. J. Adv. Res. Innov. Ideas Educ.* **2016**, *2*, 530–534.
7. Jena, S.; Sahoo, S.; Panigrahi, C.K. Effect of irradiance onyield factor of solar photovoltaic plant-A case study. In Proceedings of the 2017 International Conference on Innovative Mechanisms for Industry Applications, Bangalore, India, 21–23 February 2017; pp. 597–601.
8. Razak, A.; Yusoff, M.I.; Zhe, L.W.; Irwanto, M.; Ibrahim, S.; Zhafarina, M. Investigation of the Effect Temperature on Photovoltaic (PV) Panel Output Performance. *Int. J. Adv. Sci. Eng. Inf. Technol.* **2016**, *6*, 682–688. [CrossRef]
9. Anjum, M.B.; Khan, Q.; Ullah, S.; Hafeez, G.; Fida, A.; Iqbal, J.; Albogamy, F.R. Maximum Power Extraction from a Standalone Photo Voltaic System via Neuro-Adaptive Arbitrary Order Sliding Mode Control Strategy with High Gain Differentiation. *Appl. Sci.* **2022**, *12*, 2773. [CrossRef]
10. Hameed, W.I.; Saleh, A.L.; Sawadi, B.A.; Al-Yasir, Y.I.A.; Abd-Alhameed, R.A. Maximum Power Point Tracking for Photovoltaic System by Using Fuzzy Neural Network. *Inventions* **2019**, *4*, 33. [CrossRef]
11. Subudhi, B.; Pradhan, R. A Comparative Study on Maximum Power Point Tracking Techniques for Photovoltaic Power Systems. *IEEE Trans. Sustain. Energy* **2013**, *4*, 89–98. [CrossRef]

12. Bhatnagar, P.; Nema, R. Maximum power point tracking control techniques: State-of-the-art in photovoltaic applications. *Renew. Sustain. Energy Rev.* **2013**, *23*, 224–241. [CrossRef]

13. Kollimalla, S.K.; Mishra, M.K. Variable Perturbation Size Adaptive P&O MPPT Algorithm for Sudden Changes in Irradiance. *IEEE Trans. Sustain. Energy* **2014**, *5*, 718–728.

14. Loukriz, A.; Haddadi, M.; Messalti, S. Simulation and experimental design of a new advanced variable step size Incremental Conductance MPPT algorithm for PV systems. *ISA Trans.* **2016**, *62*, 30–38. [CrossRef] [PubMed]

15. Feroz Mirza, A.; Mansoor, M.; Ling, Q.; Khan, M.I.; Aldossary, O.M. Advanced variable step size incremental conductance MPPT for a standalone PV system utilizing a GA-tuned PID controller. *Energies* **2020**, *13*, 4153. [CrossRef]

16. Uswarman, R.; Munawar, K.; Ramli, M.A.M.; Bouchekara, H.R.E.H.; Hossain, M.A. Maximum Power Point Tracking in Photovoltaic Systems Based on Global Sliding Mode Control with Adaptive Gain Scheduling. *Electronics* **2023**, *12*, 1128. [CrossRef]

17. Haq, I.U.; Khan, Q.; Ullah, S.; Khan, S.A.; Akmeliawati, R.; Khan, M.A.; Iqbal, J. Neural network-based adaptive global sliding mode MPPT controller design for stand-alone photovoltaic systems. *PLoS ONE* **2022**, *17*, e0260480. [CrossRef]

18. Kharb, R.K.; Shimi, S.; Chatterji, S.; Ansari, M.F. Modeling of solar PV module and maximum power point tracking using ANFIS. *Renew. Sustain. Energy Rev.* **2014**, *33*, 602–612. [CrossRef]

19. Ali, K.; Khan, L.; Khan, Q.; Ullah, S.; Ahmad, S.; Mumtaz, S.; Karam, F.W.; Naghmash. Robust Integral Backstepping Based Nonlinear MPPT Control for a PV System. *Energies* **2019**, *12*, 3180. [CrossRef]

20. Saleem, O.; Abbas, F.; Iqbal, J. Complex fractional-order LQIR for inverted-pendulum-type robotic mechanisms—Design and experimental validation. *Mathematics* **2023**, *11*, 913. [CrossRef]

21. Saleem, O.; Shami, U.T.; Mahmood-ul-Hasan, K. Time-optimal control of DC-DC buck converter using single-input fuzzy augmented fractional-order PI controller. *Int. Trans. Elect. Energy Syst.* **2019**, *29*, e12064. [CrossRef]

22. Saleem, O.; Rizwan, M.; Khizar, A.; Ahmad, M. Augmentation of fractional-order PI controller with nonlinear error-modulator for enhancing robustness of DC-DC boost converters. *J. Pow. Electron.* **2019**, *19*, 835–845.

23. Jeba, P.; Immanuel Selvakumar, A. FOPID based MPPT for photovoltaic system. *Energy Sour. Part A Recover. Util. Environ. Eff.* **2018**, *40*, 1591–1603. [CrossRef]

24. Nasir, A.; Rasool, I.; Sibtain, D.; Kamran, R. Adaptive Fractional Order PID Controller Based MPPT for PV Connected Grid System Under Changing Weather Conditions. *J. Elect. Eng. Technol.* **2021**, *16*, 2599–2610. [CrossRef]

25. Bouakkaz, M.S.; Boukadoum, A.; Boudebbouz, O.; Fergani, N.; Boutasseta, N.; Attoui, I.; Bouraiou, A.; Necaibia, A. Dynamic performance evaluation and improvement of PV energy generation systems using Moth Flame Optimization with combined fractional order PID and sliding mode controller. *Sol. Energy* **2020**, *199*, 411–424. [CrossRef]

26. Rawat, A.; Jha, S.K.; Kumar, B.; Mohan, V. Nonlinear fractional order PID controller for tracking maximum power in photo-voltaic system. *J. Intell. Fuzzy Syst.* **2020**, *38*, 6703–6713. [CrossRef]

27. Saleem, O.; Awan, F.G.; Mahmood-ul-Hasan, K.; Ahmad, M. Self-adaptive fractional-order LQ-PID voltage controller for robust disturbance compensation in DC-DC buck converters. *Int. J. Numer. Model.* **2020**, *33*, e2718. [CrossRef]

28. Bellia, H.; Youcef, R.; Fatima, M. A detailed modeling of photovoltaic module using MATLAB. *NRIAG J. Astron. Geophys.* **2014**, *3*, 53–61. [CrossRef]

29. Omar, M.A.; Mahmoud, M. Design and simulation of DC/DC boost converter with maximum power point tracking for grid connected PV inverter considering the nonlinearity of the PV generator. *Int. J. Energy Convers.* **2019**, *7*, 241–252. [CrossRef]

30. Gaboriault, M.; Notman, A. A high efficiency, non-inverting, buck-boost DC-DC converter. In Proceedings of the Annual IEEE Applied Power Electronics Conference and Exposition, Anaheim, CA, USA, 22–26 February 2004; pp. 1411–1415.

31. Hagan, M.T.; Demuth, H.B.; Beale, M.H.; Jesus, O.D. *Neural Network Design*; PWS Publishing Co.: Boston, MA, USA, 1996; Volume 20.

32. Li, Z.; Liu, L.; Dehgan, S.; Chen, Y.Q.; Xue, D. A review and evaluation of numerical tools for fractional calculus and fractional order controls. *Int. J. Control.* **2017**, *90*, 1165–1181. [CrossRef]

33. Hui, P.; Ping, W.; Weihua, L. Model based fractional order pid controller design and simulation of pressure swing adsorption. In Proceedings of the 38th Chinese Control Conference (CCC), Guangzhou, China, 27–30 July 2019; pp. 2880–2883.

34. Saleem, O.; Mahmood-Ul-Hasan, K. Adaptive collaborative speed control of PMDC motor using hyperbolic secant functions and particle swarm optimization. *Turkish J. Electr. Eng. Comput. Sci.* **2018**, *26*, 1612–1622.

35. Saleem, O.; Rizwan, M. Performance optimization of LQR-based PID controller for DC-DC buck converter via iterative-learning-tuning of state-weighting matrix. *Int. J. Numer. Model.* **2019**, *32*, e2572. [CrossRef]

36. Kondawar, S.S.; Vaidya, U.B. A Comparison of two MPPT techniques for PV system in Matlab/Simulink. *Int. J. Eng. Res. Dev.* **2012**, *2*, 73–79.

37. Daraban, S.; Petreus, D.; Morel, C. A novel MPPT (maximum power point tracking) algorithm based on a modified genetic algorithm specialized on tracking the global maximum power point in photovoltaic systems affected by partial shading. *Energy* **2014**, *74*, 374–388. [CrossRef]

38. Yang, B.; Zhu, T.; Wang, J.; Shu, H.; Yu, T.; Zhang, X.; Yao, W.; Sun, L. Comprehensive overview of maximum power point tracking algorithms of PV systems under partial shading condition. *J. Clean. Prod.* **2020**, *268*, 121983. [CrossRef]